Received: 5 May 2022 | Revised: 13 September 2022 | Accepted: 18 September 2022 | Published on: 6 November 2022

DOI: 10.1002/qj.4386

Quarterly Journal of the Royal Meteorological Society RMetS

RESEARCH ARTICLE

Probing eddy size and its effective mixing length in stably stratified roughness sublayer flows

Olli Peltola[1,2] | **Mika Aurela**[2] | **Samuli Launiainen**[1] | **Gabriel Katul**[3]

[1]Natural Resources Institute Finland, Helsinki, Finland

[2]Finnish Meteorological Institute, Helsinki, Finland

[3]Department of Civil and Environmental Engineering, Duke University, Durham, North Carolina

Correspondence
Olli Peltola, Natural Resources Institute Finland, Latokartanonkaari 9, Helsinki 00790, Finland.
Email: olli.peltola@luke.fi

Funding information
Academy of Finland, Grant/Award Numbers: 296116, 315424; National Science Foundation, Grant/Award Numbers: NSF-AGS-2028633, NSF-IOS-1754893; U.S. Department of Energy, Grant/Award Number: DE-SC0022072

Stably stratified roughness sublayer flows are ubiquitous yet remain difficult to represent in models and to interpret using field experiments. Here, continuous high-frequency potential temperature profiles from the forest floor up to 6.5 times the canopy height observed with distributed temperature sensing (DTS) are used to link eddy topology to roughness sublayer stability correction functions and coupling between air layers within and above the canopy. The experiments are conducted at two forest stands classified as hydrodynamically sparse and dense. Near-continuous profiles of eddy sizes (length scales) and effective mixing lengths for heat are derived from the observed profiles using a novel conditional sampling approach. The approach utilizes potential temperature isoline fluctuations from a statically stable background state. The transport of potential temperature by an observed eddy is assumed to be conserved (adiabatic movement) and we assume that irreversible heat exchange between the eddy and the surrounding background occurs along the (vertical) periphery of the eddy. This assumption is analogous to Prandtl's mixing-length concept, where momentum is transported rapidly vertically and then equilibrated with the local mean velocity gradient. A distinct dependence of the derived length scales on background stratification, height above ground, and canopy characteristics emerges from the observed profiles. Implications of these findings for (1) the failure of Monin–Obukhov similarity in the roughness sublayer and (2) above-canopy flow coupling to the forest floor are examined. The findings have practical applications in terms of analysing similar DTS data sets with the proposed approach, modelling roughness sublayer flows, and interpreting nocturnal eddy covariance measurements above tall forested canopies.

KEYWORDS
canopy, DTS, length scale, mixing length, roughness sublayer, stable stratification, turbulence

1 | INTRODUCTION

Stably stratified atmospheric flows over rough surfaces are ubiquitous yet remain a challenge for numerical weather prediction (NWP) models (Sandu *et al.*, 2013; Edwards *et al.*, 2020; Maroneze *et al.*, 2020) and micrometeorological data interpretation alike (Cava *et al.*, 2004; Aubinet, 2008; Peltola *et al.*, 2021b). This

challenge is attributed to complex interactions between static stability damping turbulence in the vertical direction and mechanical processes that govern generation of turbulent kinetic energy (TKE) along the planar flow component. For wall-bounded flows in very stable conditions, turbulent eddies are not in direct contact with the surface (i.e., "z-less" stratification regime) and the distance from the boundary z is no longer a governing length scale describing eddy diffusivity. As such, one of the main tenets of canonical turbulent boundary layers, the Townsend attached eddy hypothesis (Katul *et al.,* 2014; Marusic and Monty, 2019), breaks down. However, a description of dominant eddy sizes and their variation with thermal stratification remains necessary for the success of NWP, since many of the NWP models still utilize Monin–Obukhov (M–O) similarity theory (Edwards *et al.,* 2020) or other parameterisations relying on mixing lengths (Maroneze *et al.,* 2020).

In the roughness sublayer within and above canopies, these difficulties are further compounded by the emergence of other length scales such as the canopy height h or the adjustment length scale (Brunet, 2020). In the absence of thermal stratification, canopy flows already differ from boundary-layer flows due to the presence of a vertically distributed momentum drag imposed by the leaves, branches, and stems on the flow. For dense canopies, the drag creates an inflection point in the mean velocity profile near $z/h = 1$ that results in generation of Kelvin–Helmholtz instabilities (Raupach *et al.,* 1996; Katul *et al.,* 1998; Finnigan, 2000; Finnigan *et al.,* 2009; Brunet, 2020). These coherent patterns are mixing-layer type eddies (Raupach *et al.,* 1996) and prevail in the roughness sublayer for momentum, heat, and scalar exchanges, including biologically active and chemically reactive scalars discussed elsewhere (Katul *et al.,* 1998). Their size scales with the so-called canopy shear length scale instead of z (Raupach *et al.,* 1996; Poggi *et al.,* 2004; Thomas and Foken, 2007). Thus, it has been conjectured that effective eddy sizes in stably stratified canopy flows result from some combination of the processes described above (shear length scale, stability-inhibiting vertical motions, and z). First-order turbulence closure schemes representing some of these effects as modifications to M–O relations and relying on characteristic mixing lengths have been developed (Harman and Finnigan, 2007; 2008) and implemented recently in land surface (Bonan *et al.,* 2018; Abolafia-Rosenzweig *et al.,* 2021) and NWP models (Lee *et al.,* 2020). However, numerous theoretical and experimental issues remain to be uncovered about the processes governing these length scales in stable to very stable canopy flows and motivate the work here.

Direct estimation of vertical length scales of eddies from micrometeorological observations remains scarce (Gao *et al.,* 1989; Cava *et al.,* 2006; Salesky *et al.,* 2013; Li, 2021). More common are length scales estimated in the streamwise direction based on time series obtained at a specific height above ground aided by Taylor's frozen turbulence hypothesis. Distributed temperature sensing (DTS; Thomas and Selker (2021)) may allow directly inferring vertical length scales in stably stratified canopy flows. Here, continuous turbulence profiles interrogated with DTS, extending from the forest floor up to $6.5h$, are utilized in two forest stands. The experiments here cover the canopy sublayer (CSL, $z/h \leq 1$), the roughness sublayer (RSL, $z/h \leq 2$–5), and the atmospheric surface layer (ASL, $z/h \geq 2$–5 and $z \leq 0.1\delta_{\mathrm{ABL}}$, where δ_{ABL} is the boundary-layer height) where M–O similarity is expected to hold for near-neutral, mildly stable, and unstable atmospheric stability conditions. There is considerable variability in RSL height estimates in the literature. For instance, wind-tunnel experiments determine RSL as $z/h \leq 2$ for momentum and ≤ 5 for heat (Raupach and Thom, 1981), whereas a recent review determines the RSL height to be z/h between 2 and 3 (Brunet, 2020) .

The focus of the DTS-based high-frequency air temperature profiles is to explore characteristic eddy sizes and effective mixing-length properties in stably stratified flows within and above sparse (Sodankylä) and dense (Hyytiälä) coniferous forests in Finland. The estimated vertical length scales are then compared against formulations in the literature, and RSL corrections to M–O similarity proposed. The implications of how turbulent length scales impact coupling between air layers within and above the canopy are also analysed.

2 | THEORY

2.1 | Experimental estimation of eddy dimensions

The dimensions of a characteristic overturning eddy in a stably stratified atmosphere are derived using spatially continuous high-frequency potential temperature (θ) profiles. Figure 1 shows schematically how overturning eddies wrap background θ isolines and how the length scales related to the eddies can be delineated by following the vertical displacement of the θ isolines. Consider an air parcel displaced vertically by the overturning eddy. It is assumed that during the ascending/descending phase of the eddy the air parcel does not exchange heat with the surroundings (i.e., θ is a conserved variable during ascent/descent and $D\theta/Dt \approx 0$ within the air parcel), but heat exchange takes place only after the air parcel has been displaced by a certain length that is relative to the vertical size of the eddy. This is akin to Prandtl's mixing-length hypothesis (Prandtl, 1925). In the case in which there is noticeable

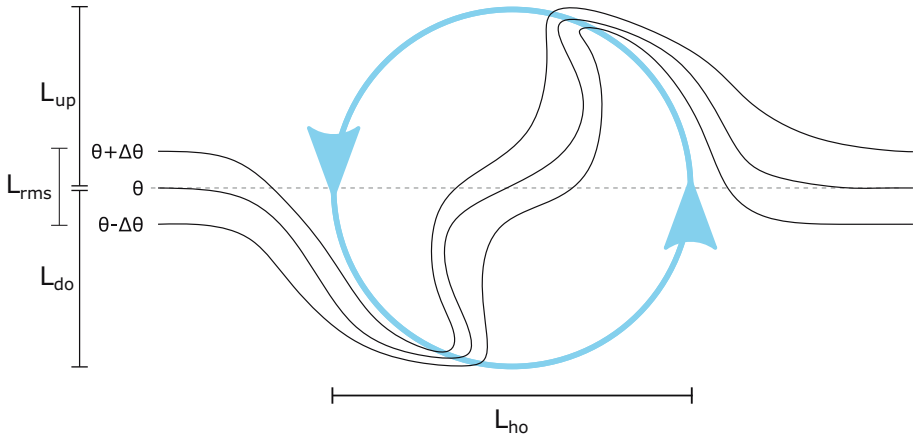

FIGURE 1 Schematic figure showing an idealized overturning eddy in a stratified flow (Ivey *et al.*, 2000), along with a description of how it wraps potential temperature (θ) isolines (black lines). L_{up}, L_{do}, and L_{ho} describe the vertical up, vertical down, and horizontal dimensions of the eddy, respectively, and L_{rms} describes the effective vertical mixing length [Colour figure can be viewed at wileyonlinelibrary.com]

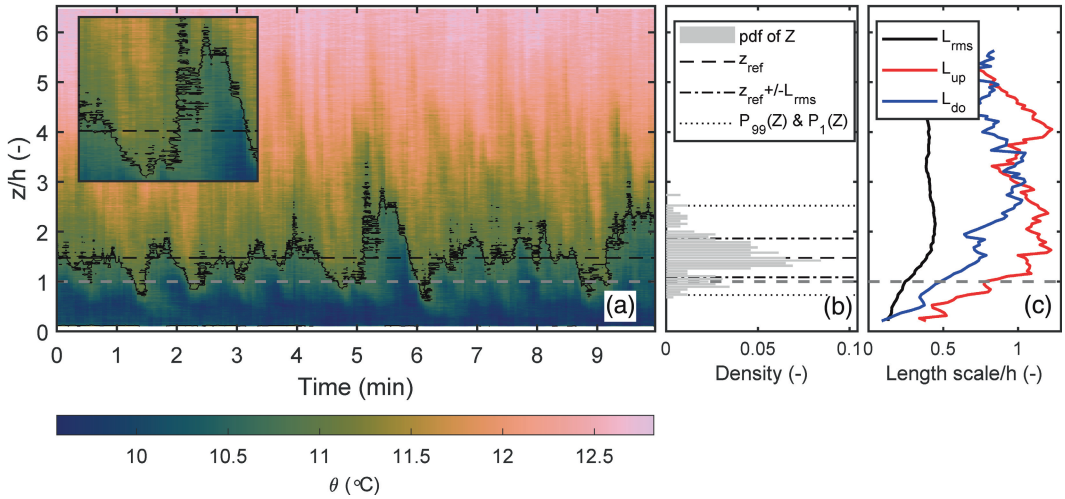

FIGURE 2 Example of how the three length scales (L_{up}, L_{do}, and L_{rms}) were derived from continuous θ profiles measured with DTS. (a) Time series of θ profiles measured at the Hyytiälä station during an example 10-min period (2320–2330 UTC+2 on June 28, 2019). The continuous black line shows the θ isoline for average θ (θ_{ref}) observed at z_{ref} = 1.5 h (black dashed line). The inset highlights the eddy fingerprint in the θ isoline fluctuations (between 4 and 6 mins); note the similarity between the inset and Figure 1. (b) Probability density function of Z (height of θ_{ref} isoline) during the example 10-min period shown in (a). The three length scales (L_{up}, L_{do}, and L_{rms}) were calculated from this distribution (Equations 1–3) and they characterise the shape of the distribution at this particular height (z_{ref}). (c) A similar distribution was calculated throughout the θ profile and continuous profiles for L_{up}, L_{do}, and L_{rms} were derived from these distributions. The horizontal grey dashed line is the canopy height ($z/h = 1$) [Colour figure can be viewed at wileyonlinelibrary.com]

heat exchange between the air parcel and the surrounding air during the ascent/descent, then the eddy dimensions derived using the θ isolines will be smaller than the actual eddy size. In practise, four length scales are computed from the space–time distribution of θ measured by DTS:

$$L_{up} = P_{99}(Z) - \overline{Z}, \tag{1}$$

$$L_{do} = \overline{Z} - P_1(Z), \tag{2}$$

$$L_{rms} = \sqrt{\overline{Z'Z'}}, \tag{3}$$

$$L_{ho} = U_{adv}\tau_Z, \tag{4}$$

where Z is the height of the θ isoline as it fluctuates vertically, primes ($'$) denote fluctuation around a mean that is denoted with an overbar $\overline{()}$, P is the percentile function (e.g., $P_1(Z)$ is the first percentile of Z values), τ_Z is the integral time scale of the Z time series and U_{adv} is the eddy advection velocity. To evaluate these length scales, $\overline{\theta}$ profiles are first computed from the vertically continuous θ profiles for each averaging period. Next, Z is determined by following how these $\overline{\theta}$ values fluctuate vertically within the averaging period. To make the determination of Z fluctuations robust, spline fit to the θ profiles are used to smooth out noise in the θ profiles prior to estimating Z for each time step. This procedure provides continuous profiles of Z time series that enable the estimation

of continuous profiles of the length scales (see Figure 2). As such, L_{rms} can be considered to describe the effective mixing length related to the overturning eddy and L_{do} and L_{up} describe the vertical dimension of the eddy. If Z follows a Gaussian distribution, then $L_{rms} \approx (L_{up} + L_{do})/4.65$ and $L_{up} \approx L_{do}$. The horizontal scale of the eddy (L_{ho}) is derived by estimating the integral time scale of Z by integrating its autocovariance function up to the first zero crossing and then converting the obtained time scale to a length scale by assuming Taylor's frozen turbulence hypothesis and a constant U_{adv} throughout the profile (wind speed above canopy). The proposed approach to derive the length scales (Equations 1–3) holds similarities to the Thorpe length scale estimated from individual θ profiles (Thorpe, 1977; Moum, 1996; Smyth and Moum, 2000; Lorke and Wüest, 2002; Sorbjan and Balsley, 2008).

2.2 | Relating the estimated length scales to M–O theory and RSL flow via Prandtl mixing-length concept

Using Prandtl's mixing-length hypothesis, a characteristic mixing length can be defined from

$$\theta' = -l'_h \frac{\partial \overline{\theta}}{\partial z}, \qquad u' = -l'_m \frac{\partial \overline{u}}{\partial z}, \tag{5}$$

where u is the horizontal velocity aligned with the mean wind during a certain averaging period, and l'_h and l'_m are vertical distances over which heat and momentum, respectively, are transported. They fluctuate in a manner similar to θ' and u' by this definition. Equation (5) states that the turbulent fluctuations (θ' and u') are proportional to the mean vertical gradients ($\partial\overline{\theta}/\partial z$ and $\partial\overline{u}/\partial z$) and the vertical distance over which tagged air parcels are displaced (l'_h and l'_m). This follows from the assumption that the air parcel carries the mean properties of its original position over a characteristic vertical distance (l'_h or l'_m) prior to blending with the mean flow (Section 2.1). The turbulent vertical wind speed w' simply acts to displace the tagged air parcels randomly up or down along these mean gradients. In this study, the w' (magnitude or sign) is not defined by the mean gradients in longitudinal velocity, as typically done when utilizing the mixing-length hypothesis. Instead, its root-mean-squared value is given by $\sigma_w = (\overline{w'^2})^{1/2}$. With these definitions, the turbulent fluxes $\overline{w'\theta'}$ and $\overline{w'u'}$ can be expressed as

$$\overline{w'\theta'} = -r_h \sigma_w L_h \frac{\partial \overline{\theta}}{\partial z}, \qquad \overline{w'u'} = -r_m \sigma_w L_m \frac{\partial \overline{u}}{\partial z}, \tag{6}$$

where r_h (r_m) is the correlation coefficient between w' and l'_h (l'_m), and L_h and L_m are the root-mean-squared values of l'_h and l'_m, respectively. The correlation coefficient between two flow variables s_1 and s_2 is $r = \overline{s'_1 s'_2}(\sigma_{s1}\sigma_{s2})^{-1}$. The turbulent Prandtl number (Pr_t) can be written based on the heat eddy diffusivity ($K_h = r_h \sigma_w L_h$) and the turbulent viscosity ($K_m = r_m \sigma_w L_m$) as

$$Pr_t = \frac{K_m}{K_h} = \frac{r_m}{r_h}\frac{L_m}{L_h}. \tag{7}$$

The exact values for r_h and r_m are still unknown, but only their ratio is of relevance here. These correlation coefficients are bounded between 0 and 1, since w' and l'_h (l'_m) are positively correlated (i.e., updrafts/downdrafts create positive/negative mixing-length fluctuations). Considering that θ' and l'_h are linearly proportional to each other (Equation 5), r_h could be conjectured to be equal to the correlation coefficient between w' and θ' (r_θ) and the same reasoning applies for the correlation between w' and l'_m and w' and u' (r_u). However, likely $r_h > r_\theta$ and $r_m > r_u$, since l'_h and l'_m are directly related to the active vertical turbulent transport, whereas θ' and u' contain inactive turbulent motions not directly related to vertical transport (but contribute to variances) and hence these motions decrease the observed r_θ and r_u. It is shown in Appendix S1 that in near-neutral conditions $r_m \approx 1/\phi_w$, where $\phi_w = \sigma_w/u_*$ and u_* is friction velocity ($u_* = \sqrt{-\overline{w'u'}}$) and $r_h \approx 1/(\phi_w \phi_\theta)$, where $\phi_\theta = \sigma_\theta/\theta_*$, σ_θ is the standard deviation of θ fluctuations, and θ_* is the temperature scale ($\theta_* = |\overline{w'\theta'}/u_*|$). These values are also consistent with other recent studies (Basu and Holtslag, 2021). As r_θ, r_u, ϕ_w, and ϕ_θ are all relatively constant in a stable boundary layer (Kaimal and Finnigan, 1994), the variability of K_h and K_m with stability is likely to be driven by σ_w or the length scales L_h and L_m. From this, it also follows that the variability of Pr_t in the stable boundary layer is dictated by the ratio of momentum and heat length scales (L_m/L_h).

M–O similarity theory (Monin and Obukhov, 1954) describes the nondimensional θ and u gradients as universal functions of a stability parameter $\zeta = (z-d)/L$:

$$\phi_h(\zeta) = \frac{\kappa(z-d)}{\theta_*}\frac{\partial \overline{\theta}}{\partial z}, \qquad \phi_m(\zeta) = \frac{\kappa(z-d)}{u_*}\frac{\partial \overline{u}}{\partial z}, \tag{8}$$

where κ is the von Karman constant, z is the height above ground, d is the zero-plane displacement height introduced by the canopy ($d = 0.7h$ is assumed throughout), and L is the Obukhov length defined using measured turbulent heat and momentum fluxes above the canopy. Now by utilizing Equation (6) and reorganising, these stability

correction functions can be expressed as

$$\phi_h = \frac{\kappa(z-d)}{r_h \phi_w L_h}, \qquad \phi_m = \frac{\kappa(z-d)}{r_m \phi_w L_m}. \tag{9}$$

Noting that r_h, ϕ_w, and r_m are all relatively constant with stability (Kaimal and Finnigan, 1994), the M–O similarity functions (ϕ_h and ϕ_m) can be regarded as functions describing the decrease in eddy size as stability inhibits vertical mixing ($\phi_h \propto \kappa(z-d)/L_h$).

In an effort to extend the M–O similarity theory to the roughness sublayer, the dimensionless similarity functions are typically multiplied by a correction function (ϕ^*) describing the effect of roughness elements on the dimensionless gradients (Equation 8: Garratt, 1980; Physick and Garratt, 1995; Mölder *et al.,* 1999; Harman and Finnigan, 2007; 2008; Arnqvist and Bergström, 2015; Brunet, 2020). Using this extension,

$$\phi_h = \phi_h^{MO} \phi_h^*, \qquad \phi_m = \phi_m^{MO} \phi_m^*, \tag{10}$$

where ϕ_h^{MO} and ϕ_m^{MO} follow M–O similarity theory and the RSL correction functions can be defined as

$$\phi_h^* = \frac{L_h^{MO}}{L_h}, \qquad \phi_m^* = \frac{L_m^{MO}}{L_m}, \tag{11}$$

where L_h^{MO} and L_m^{MO} are the length scales based on M–O theory (e.g., $L_h^{MO} = \kappa(z-d)/\left[r_h \phi_w \phi_h^{MO}\right]$) and L_h and L_m are the observed length scales. Note that above RSL and within ASL $\phi_h^* = \phi_m^* = 1$, since $L_h = L_h^{MO}$ and $L_m = L_m^{MO}$. Hence, the RSL correction functions describe how the observed length scales deviate from the M–O predicted values in the RSL. Considering Equation (11) and the fact that, within the RSL, $\phi_h^* < 1$ and $\phi_m^* < 1$ suggests that roughness sublayer eddies appear larger than predicted with M–O theory at the same distance from the zero-plane displacement ($z-d$).

2.3 | Reference length scales

We compare the length scales estimated from the DTS profiles (Section 2.1) against streamwise integral length scales of w (L_w):

$$L_w = U_{adv} \tau_w, \tag{12}$$

where U_{adv} is the mean wind speed measured with the sonic anemometer also measuring the w time series and τ_w is the integral time scale of the high-frequency w time series. Similarly to the case of L_{ho} (Equation 4), τ_w is derived by integrating the w time series autocovariance function up to the first zero-crossing. L_w relates to the size of active eddies and hence is a suitable point of comparison for the length scales derived from the DTS profiles.

Additionally, the length scales are also compared against the buoyancy length scale (L_b):

$$L_b = \frac{\sigma_w}{N}, \tag{13}$$

where N is the Brunt–Väisälä frequency calculated using $\partial\overline{\theta}/\partial z$ derived from the DTS $\overline{\theta}$ profile. L_b relates to the vertical distance over which vertically displaced air parcels travel if their kinetic energy is completely transformed to potential energy (Sorbjan, 2006; Basu and Holtslag, 2021).

2.4 | Decoupling metric Ω

A decoupling metric Ω for evaluating whether the turbulent flow at a specific height above ground is coupled with the ground below is described elsewhere (Peltola *et al.,* 2021b). The derivation was based on the idea that, in coupled flow, strong downdrafts are able to penetrate through the stable air layers and forest canopy and couple directly with the ground below. In other words, during coupling the kinetic energy of the downdrafts is larger than (or equal to) the work done against buoyancy and canopy drag force during the descent. Based on this, Ω was defined as

$$\Omega = \frac{\sigma_w}{|w_{e,crit}|}, \tag{14}$$

where $w_{e,crit}$ is the critical downward speed of the air parcel just large enough to overcome the hindrances to downward movement during the vertical trajectory (i.e., buoyancy and canopy drag force). Using extensive data, it was shown that the flow is coupled with the ground when $\Omega > 0.61$ (Peltola *et al.,* 2021b). Assuming a Gaussian distribution for w' fluctuations, this limit corresponds to the fact that 5% of w' fluctuations are strong enough to reach and interact with the ground. When calculating $w_{e,crit}$, the value for the drag coefficient was revised to 0.2, whereas the other parameter needed in the calculation (which describes wind speed and σ_w profiles below h) was taken directly from Peltola *et al.* (2021b). Plant-area indices (PAIs) and canopy heights used in the calculations are provided in Table 1.

3 | EXPERIMENTS

The two measurement sites here are located in Scots pine (*Pinus Sylvestris L.*) dominated forest stands in Finland (Table 1). Observations on forest–atmosphere interactions have been carried out for decades at both sites and they

TABLE 1 Description of the two measurement sites included in this study

	Hyytiälä	Sodankylä
Latitude (°N)	61.85	67.36
Longitude (°E)	24.28	26.64
Measurement period (dd/mm/yyyy)	25/05/2019–10/07/2019	03/06/2020–20/12/2020
Mast height (m)	125	48
Canopy height, h (m)	19	12
Plant-area index, PAI ($m^2 \cdot m^{-2}$)	3	1.2
Air temperature (°C)	14.3 (4.329.2)	7.3 (−26.3 to 26.9)
Dominant tree species	Scots pine	Scots pine

Note: Plant-area index (PAI) refers to projected PAI. Air temperature refers to mean (min to max) value observed approximately 1 m above ground during the two measurement campaigns.

belong to several international measurement networks such as Integrated Carbon Observation System (ICOS). Hyytiälä forest is a typical managed coniferous forest: the Scots pines are even-aged (planted in 1962), the canopy coverage and tree height around the measurement mast are relatively uniform. Understorey trees with diameter <5 cm were removed from the site at the beginning of summer 2019. Due to this, an exact estimate for the forest projected PAI during summer 2019 is not available, but based on Kolari *et al.* (2022) we approximate it to be 3 $m^2 \cdot m^{-2}$. The site is located on slightly hilly terrain. See more details of Hyytiälä forest in Kolari *et al.* (2022). In contrast, Sodankylä forest is patchy, more sparse than Hyytiälä and located on flat terrain. The forest has not been managed and has regenerated naturally after forest fires. Tree age around the measurement mast ranges between 80 and 100 years. There is considerable variation in tree height due to isolated tall trees. Projected PAI was estimated with fisheye imagery to be 1.2 $m^2 \cdot m^{-2}$. Based on the Brunet (2020) classification, Hyytiälä can be considered as dense and Sodankylä as sparse forest.

The Hyytiälä experiments were conducted during the summer of 2019 (May 25–July 10) at a 127-m tall mast. The measurement setup is described elsewhere (Peltola *et al.*, 2021a; 2021b) and only salient details are given here. Two triaxial sonic anemometers (HS-50, Gill Instruments Limited, UK and USA-1, manufactured by METEK Meteorologische Messtechnik GmbH, Germany) measured the three velocity components and sonic temperature at 10 Hz. The sonic anemometers were positioned at 27 m (1.4h) and 68 m (3.6h) above the ground, respectively.

A thin (0.9 mm outer diameter), white multimode aramid-reinforced 50-μm fibre-optic cable (AFL Telecommunications LLC, Duncan, SC 29334, US) was attached to the tall mast with 0.5-m long horizontal booms (see Figure 3 for a schematic description of the configuration). The total length of the cable was approximately 362 m. The cable started and ended next to the DTS instrument (ULTIMA-S, 5-km variant; Silixa Ltd, Hertfordshire, UK) and hence this setup allowed double measurement of the vertical θ profile with 12.7-cm spatial and 1-Hz temporal resolution. Both ends of the cable were attached to the DTS instrument (i.e., double-ended configuration) on June 3, but before that only one end of the cable was attached (i.e., single-ended configuration). Two 50-l cooler tanks were filled with water and used as calibration baths (warm and cool baths). The cable was guided through the baths from both ends of the cable, resulting in four calibration sections. The bath temperatures were controlled with two thermostats (RC 6 CS, Lauda Dr. R. Wobser GmbH & Co. KG, Domicile Lauda–Königshofen, Germany) and they were set to 5 and 30°C. The calibration bath water temperatures were monitored with pt-100 thermistors supplied with the DTS instrument.

The Sodankylä measurements were conducted with double-ended DTS configuration at the 48-m tall mast continuously for approximately 6 months during the year 2020 (June 3–December 20). The total length of the fibre-optic cable was 291 m. The Sodankylä DTS measurement setup was identical to the Hyytiälä setup, except that the calibration baths were arranged differently. At the beginning of the measurement campaign (until August 22), the 50-l cooler tank ("warm bath") was situated outside the measurement cabin (that housed the DTS instrument) and the water temperature was kept above ambient with a heater cable at the bottom of the water tank. On August 22, the tank was moved indoors and heating was removed. After this, water temperature matched indoor air temperature and was above the outdoor ambient temperature. The internal bath of the Lauda thermostat (ECO RE 620 S, Lauda Dr. R. Wobser GmbH & Co. KG, Domicile Lauda–Königshofen, Germany) was used as a "cold bath".

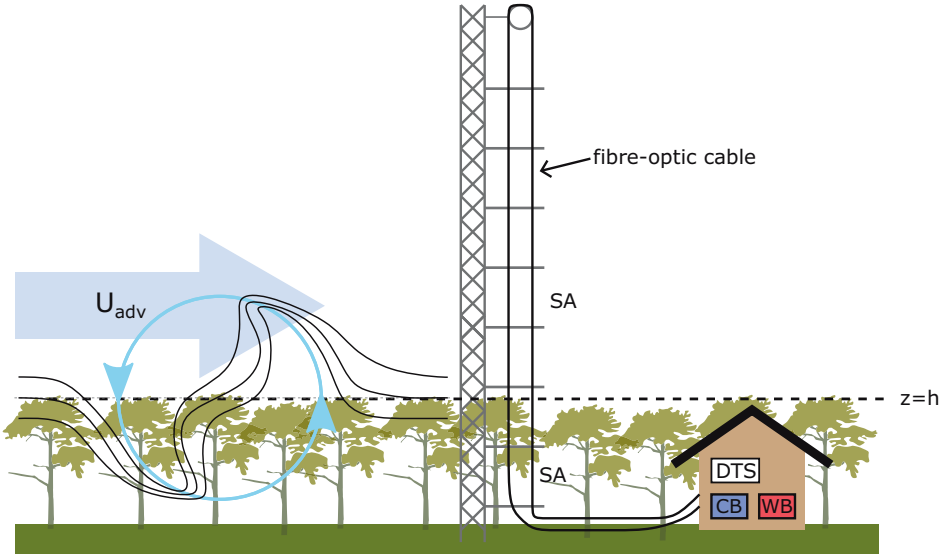

FIGURE 3 Schematic figure showing the measurement setup at the two measurement sites. A characteristic eddy (Figure 1) and the velocity (U_{adv}) at which it is advected past the tower are also depicted on the left. CB, cold calibration bath; DTS, DTS instrument; SA, sonic anemometer; WB, warm calibration bath [Colour figure can be viewed at wileyonlinelibrary.com]

The bath volume is approximately 5 l, but the thermostat controls the liquid temperature rigorously and hence the internal bath is a suitable location for DTS calibration despite its limited volume. At first, the thermostat tank was filled with water and set to 5°C. On November 26, water was replaced with cooling liquid and the liquid temperature was set to −15°C. This way the cold bath was also below the outdoor ambient temperature most of the time in wintertime freezing conditions. Warm-bath temperature was monitored with a pt-100 thermistor, whereas cold-bath liquid temperature was assumed to match the operating temperature setpoint of the thermostat. The 3D sonic anemometers (USA-1, METEK Meteorologische Messtechnik GmbH, Germany), situated at 24.5 and 3 m above the ground (2.0h and 0.3h, respectively), were sampling at 10 Hz.

3.1 | Data processing

The DTS measurements were post-field calibrated using the reference temperature data from the calibration baths, Stokes (P_S) and anti-Stokes (P_{aS}) signals recorded with the DTS instrument and the following equation (van de Giesen *et al.*, 2012):

$$T(x,t) = \frac{\gamma}{\ln \frac{P_S(x,t)}{P_{aS}(x,t)} + C(t) + \int_0^x \Delta\alpha(x')dx'}, \qquad (15)$$

where T is the calibrated temperature as a function of position along the cable (x) and time (t), C is a time-dependent calibration parameter (constant along the cable), γ is assumed constant (Peltola *et al.*, 2021a), and the integral in the denominator describes the differential attenuation of the Stokes and anti-Stokes signals along the cable. The double-ended configuration enabled exact estimation of the differential attenuation for each location along the cable (van de Giesen *et al.*, 2012). For the single-ended configuration used at the beginning of the Hyytiälä measurements, the term was estimated using the calibration bath sections at the beginning and end of the cable. Following des Tombe *et al.* (2020), the parameter C was estimated separately for the forward and reverse signals. After obtaining the high-frequency C time series, they were low-pass filtered (simple moving average with 100-s window) to suppress noise in the C estimates. Then the estimated C time series, fixed value for γ, and differential attenuation vector were used in Equation (15) to estimate T along the cable for each time step. This was done separately for the forward and reverse measurements. As the DTS instrument performs the measurements in forward and reverse directions sequentially, the T data stemming from the reverse measurements were linearly interpolated in time to match the time stamps for the forward measurements and then averaged to yield continuous T data along the cable with 0.5-Hz temporal and 0.127-cm spatial resolution. Finally, the T profiles along the tower were extracted from the T data along the cable, and the two T profiles (from the cable going up and down the masts) were averaged and then converted to θ profiles using the dry adiabatic lapse rate. To suppress noise in the DTS-derived θ profiles, they were denoised using an algorithm based on singular-value decomposition. Here, a variant of the Epps and Krivitzky (2019) algorithm was used (Karttunen *et al.*, 2022). These denoised θ profiles were used to derive the turbulence length scales using the procedure outlined in Section 2.1.

High-frequency wind and temperature data from the sonic anemometers were despiked following Brock (1986) and the coordinate frame was rotated using the planar

fit algorithm (Wilczak *et al.,* 2001). Linear detrending was used to extract turbulent fluctuations from the measurements. For Hyytiälä, sonic anemometer data were removed when the wind was blowing through the measurement mast, since the turbulent flow field was disturbed, whereas for Sodankylä data similar filtering was not performed, since flow disturbance was not evident in the data.

A 10-min averaging period was used throughout the study. In order to evaluate the impact of averaging period length on the length scale estimates, Hyytiälä data were also processed with 30-min averaging. Based on this exercise, vertical length scales (L_{up}, L_{do}, and L_{rms}) were not greatly affected by the averaging period (values within 10–15%), but horizontal length scale (L_{ho}) increased more (up to 40%). We attribute this change in L_{ho} to nonstationarities and inactive eddies and due to these disturbances we opted to use 10-min averaging in this study.

DTS derived length scales L_{rms}, L_{up}, and L_{do} were removed from analysis if L_{up} reached the tower top. This removed data especially near the tower top and in near-neutral situations when the eddies are large. Additionally, periods when DTS $\overline{T}$ was biased compared with reference air temperature measurements (absolute difference above 1°C) were removed, as during these periods there were difficulties in DTS calibration. Also, periods when $\partial\overline{\theta}/\partial z$ calculated over the whole vertical column was less than 0.002 K·m^{-1} were removed from the analysis. The rationale is that the method used to derive the length scales here depends on tracking θ isolines over a finite and measurable vertical θ gradient. The outcome of this data filtering is that the amount of data available for analyses decreases with height and increases with stability (Figure 4). Throughout the study, bin-averaging of data was done only if less than 20% of the data in the bin correspond to periods during which L_{up} reaches the tower top. During these periods, eddies are large and the data samples in the bins are biased towards low values when large fractions of data are removed by the filtering prior to bin averaging. We limit the analyses to periods when above-canopy Obukhov length (L) is positive (i.e., stable cases). During summer, these conditions relate primarily to nocturnal periods, but for winter data daytime periods are also included in the analyses.

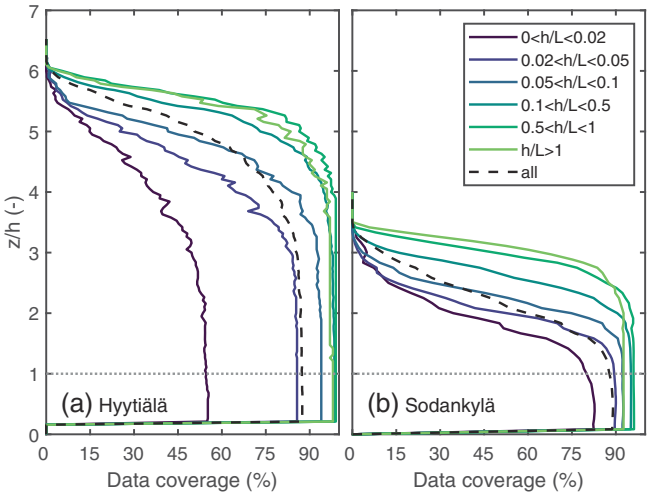

FIGURE 4 Length scale data coverage in h/L bins. Here, binning was based on L measured above the canopy ($z/h = 1.4$ in Hyytiälä and $z/h = 2.0$ in Sodankylä). The dashed line shows the overall data coverage when $h/L > 0$ [Colour figure can be viewed at wileyonlinelibrary.com]

4 | RESULTS AND DISCUSSION

4.1 | Comparison of length scales

The length scales estimated with the DTS θ profiles (Equations 1–3) are first compared against conventional estimates for turbulence length scales so as to relate them to prior studies and theories. L_{rms} should presumably match with the integral length scale of w (L_w), since L_{rms} derives the vertical size of an eddy that is actively contributing to the vertical heat transport. However, L_{rms} is derived solely from θ profiles, whereas sonic anemometer data are utilized for the estimation of L_w. Based on Figure 5a,b, L_{rms} agrees with L_w above the canopy at the two pine forest sites and the majority of the data points cluster around the 1:1 line. However, in Sodankylä (Figure 5b), outliers are more frequent below than above the 1:1 line, meaning that occasionally L_w is larger than L_{rms}.

Agreement between L_{rms} and L_w in the subcanopy airspace is worse than above the canopy (compare Figure 5c and Figures 5a,b), but nevertheless the values are still of the same order of magnitude. There are at least three possible explanations for the scatter in Figure 5c. First, θ is not strictly conserved during the eddy vertical motion in the subcanopy air space, since heat exchange may take place between the eddy and the canopy elements. This would render the assumptions made in Section 2.1 invalid. Second, in stably stratified situations, the below-canopy air space is actually often neutrally stratified due to longwave radiation components smoothing vertical θ gradients (see discussion in Section 4.2). In such conditions, θ isolines fluctuate vertically over the whole subcanopy domain, whereas L_w may be affected by canopy elements breaking turbulent eddies and thus decreasing L_w. Third, there are large uncertainties in utilizing Taylor's frozen turbulence hypothesis in canopy flows (Huang *et al.,* 2009; Brunet, 2020; Everard *et al.,* 2021). Hence, estimating the

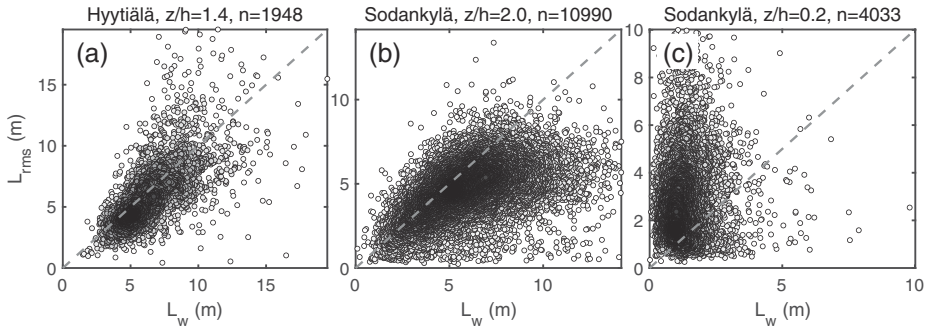

FIGURE 5 Comparison between L_{rms} and streamwise integral length scale of w (L_w) estimated using Taylor's frozen turbulence hypothesis and measured local wind speed (U_{adv}). The dashed line is the 1:1 line and marker face colours indicate density of the point cloud. The 0.5% data (outliers) were left outside the plots for clarity. The n in the subplot titles indicates the amount of data points in the plots

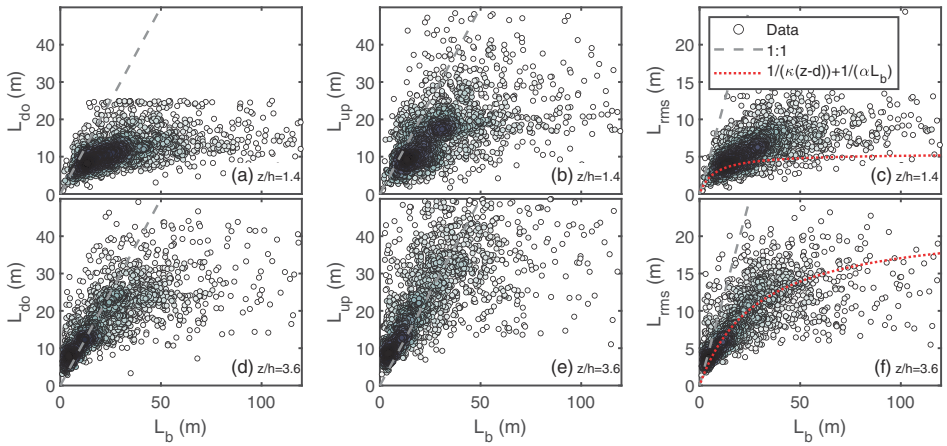

FIGURE 6 Comparison of L_{do}, L_{up}, and L_{rms} with L_b at two heights for the Hyytiälä site. Marker face colours indicate density of the point cloud. $\alpha = 0.76$ was used (Deardorff, 1980) [Colour figure can be viewed at wileyonlinelibrary.com]

integral length scale of w from time series using a mean advection velocity become problematic. Note that the estimation of L_{up}, L_{do}, and L_{rms} does not rely on Taylor's frozen turbulent hypothesis. The uncertainty related to Taylor's hypothesis also relates to the scatter in Figure 5a,b. Despite all these uncertainties, there is a direct connection between the magnitude of L_{rms} and L_w and L_{rms} is commensurate with the vertical size of an active eddy transporting heat. This is further supported with spectral analyses (Appendix S2), where it is shown that $1/L_{rms}$ and $1/L_w$ are commensurate with wavenumbers where premultiplied w power spectra peak. Therefore, the technique used to derive the length scales (Section 2.1) can be used to evaluate changes in eddy dimensions as z/h, stratification, and canopy structure change.

L_{do}, L_{up}, and L_{rms} are also compared against the estimated buoyancy length scale L_b, which can be used as a metric for maximum vertical extent of a turbulent eddy in a stably stratified environment. Figures 6a–c show the agreement between L_{do}, L_{up}, and L_{rms} with L_b slightly above the canopy and Figure 6d–f refer to data from above the RSL. At low L_b (i.e., high stratification), L_{do} values increase with L_b, however at high L_b (i.e., low stratification) L_{do} values level off (Figure 6a,d) to a constant value specific to each height. This leveling off is due to distance from the ground below setting a more stringent limit on the eddy size than L_b. At low L_b, the eddy size is dictated by stratification and not by the proximity to the ground below and hence L_{do} follows L_b. In essence, in these situations eddies are detached from the surface. L_{up} shows qualitatively similar behaviour to L_{do}, however L_{up} does not similarly level off to a constant value at high L_b, but rather continues to increase with L_b. Hence L_{up} is not similarly limited by the presence of ground below, but rather it is related more to stratification. As L_{rms} is tightly connected to L_{do} and L_{up} (see Section 2.1), it shows a L_b dependence that is an amalgam of the L_{do} and L_{up} dependences discussed above (Figure 6c,f).

In ASL and above RSL, the combined effect of distance from the ground and stratification on L_{rms} can be described utilizing a resistance in series analogue interpolation (Blackadar, 1962) as $1/L_{rms} \approx 1/(\kappa(z-d)) + 1/(\alpha L_b)$ (Figure 6f), where $\alpha = 0.76$ was taken from Deardorff (1980). Similar formulations for turbulent length scales in the SBL have been used in other models (e.g., in Brost and Wyngaard (1978); Baas *et al.* (2008); MacDonald and Teixeira (2020)). In near-neutral conditions ($\kappa(z-d) \ll L_b$), this formulation reverts to conventional surface-layer scaling (i.e., mixing length $\approx \kappa(z-d)$), whereas in strongly stable conditions ($\kappa(z-d) \gg L_b$) mixing length is proportional to L_b. In contrast to the ASL flow,

within RSL the L_{rms} estimates depart from this formulation (Figure 6c) and the values obtained in near-neutral situations are larger than predicted for ASL eddies (i.e., $L_{rms} > \kappa(z-d)$). This was expected, since RSL eddies have been found to be larger than the corresponding ASL eddies (Brunet, 2020).

4.2 | Dependence of length-scale profiles on stability

With this background, the role of atmospheric stability on length-scale profiles and eddy dimensions is now considered. Figure 7 shows the median L_{up}, L_{do}, L_{rms}, and L_{ho} profiles in h/L bins. The L_{up}, L_{do}, and L_{rms} profiles show a similar pattern at the two sites (albeit there are differences in near-neutral situations), suggestive of a wider applicability of these findings to other forests. The initial focus here is on L_{up} and L_{do} profiles (Figure 7a,b). Above the canopy, they both increase with height in the near-neutral regime and decrease with stability. $L_{up}/L_{do} > 1$ in all cases, but L_{up} decreases faster as a function of stability than L_{do}. They both attain a constant value with height ($\propto L_b$) and $L_{do}/L_{up} \approx 1$ (Figures 7a,b and 8a) for very stable conditions. These findings are qualitatively the same as the findings for vertical integral length scales for w in the up and down directions reported for ASL flow (Salesky *et al.*, 2013). They showed that the vertical integral length scale of w in the up direction was consistently larger and decreased faster with increasing stability than the length scale in the down direction. After reaching a specific stability value, the length scales in the up and down directions were similar (but not exactly the same). This can be considered as a limit for stability, above which the flow is fully decoupled from the underlying surface and length scales are governed by stability alone ("z-less" regime). These results indicate that in the near-neutral limit the eddies are elongated upwards ($L_{up} > L_{do}$), whereas in strongly stable situations they are symmetrical around their vertical position z ($L_{up} \approx L_{do}$).

We hypothesise that $L_{do}/L_{up} < 1$ in near-neutral RSL is due to the fact that in these situations the downdrafts (L_{do}) and updrafts (L_{up}) are related to different physical processes. In near-neutral conditions, L_{do} is related to attached eddies and strong downdrafts that sweep through the $z = h$ layer, whereas L_{up} is related to mixing-layer eddies generated locally at $z/h \approx 1$ by inflection-point instability. The TKE production mechanism between these two flow modes is different and hence, for example, the vertical wind-speed skewness is typically negative (downward w' fluctuations are stronger than upward fluctuations) just above the canopy (Brunet, 2020). This might also explain why the two sites differ in near-neutral conditions. The Sodankylä forest is likely too sparse to generate an inflection point in the mean wind-speed profile at $z/h \approx 1$ and hence mixing-layer eddies are not prevalent at the site, whereas the denser Hyytiälä forest is suitable for the generation of mixing-layer eddies at $z/h \approx 1$. Unfortunately, we lack the detailed mean wind-speed profiles needed for corroborating this hypothesis. Finally, it is emphasised that the estimation of length scales with

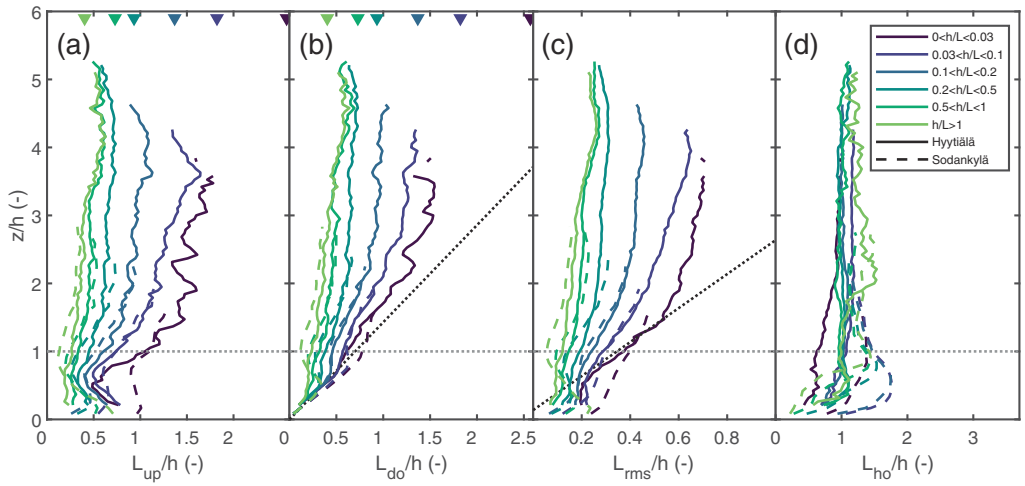

FIGURE 7 Median length-scale profiles in h/L (ratio of canopy height and Obukhov length) bins. Note the similarity between sites. The black dotted line in (b) shows $L_{do} = 0.7z$, the black dotted line in (c) shows $L_{rms} = \kappa(z-d) + c$, where c equals the median L_{rms} observed below the canopy when $0 < h/L < 0.03$. Triangles at the top of panels (a) and (b) show median L_b/h in h/L bins measured at $z/h = 1.4$ in Hyytiälä. Here, binning was based on L measured above the canopy ($z/h = 1.4$ in Hyytiälä and $z = 2.0$ in Sodankylä). Note the change in x-axis scale [Colour figure can be viewed at wileyonlinelibrary.com]

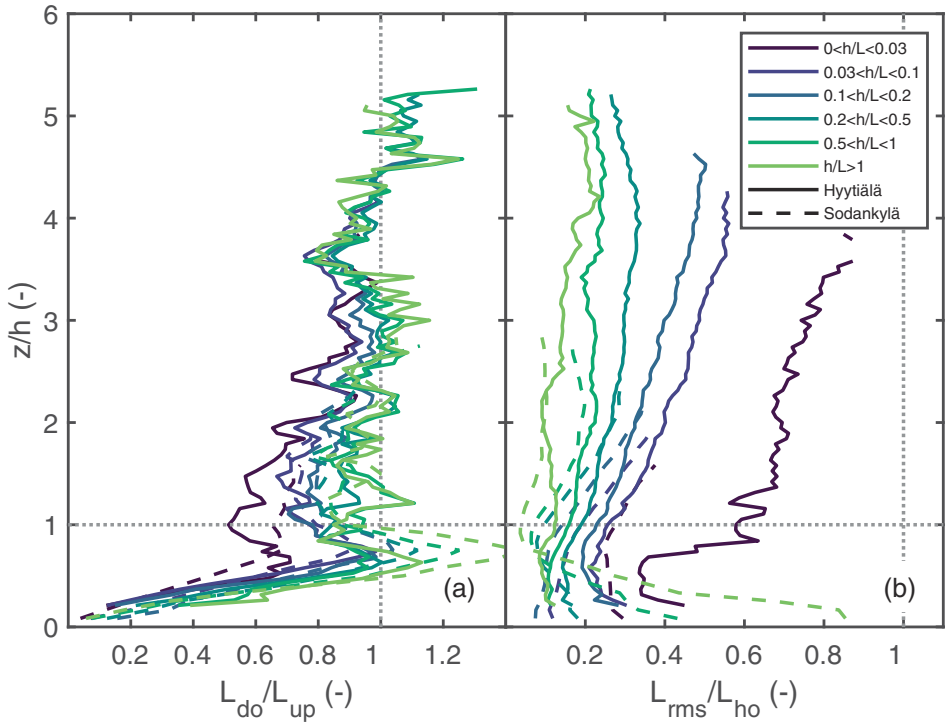

FIGURE 8 Median profiles of length scale ratios in h/L bins. Here, binning was based on L measured above the canopy ($z/h = 1.4$ in Hyytiälä and $z = 2.0$ in Sodankylä) [Colour figure can be viewed at wileyonlinelibrary.com]

the approach in Section 2.1 is uncertain in near-neutral conditions, due to small θ gradients.

Recalling that L_{rms} agrees with the streamwise integral length scale of w (L_w), Figure 7c can also be considered to depict L_w profiles. A large-eddy simulation (LES) study (Huang and Bou-Zeid, 2013) analysed L_w profiles in a stably stratified ABL and the results show similarities to the RSL findings here (i.e., L_w increases with height near the surface in near-neutral conditions and L_w decreases with stability). The observed L_{rms} profiles in near-neutral conditions are similar to reported L_w profiles in the literature (Raupach *et al.,* 1996; Brunet, 2020). Moreover, it was already reported that $L_w/h \approx 1/3$ at $z = h$ and L_w/h decreases towards approximately 0.05–0.1 (depending on forest density) when approaching the forest floor (Brunet, 2020). The near-neutral results here suggest that $L_{\mathrm{rms}}/h \approx 0.4$ at $z = h$ and $L_{\mathrm{rms}}/h \approx 0.2$ near the forest floor. These are at the upper end of the range of reported values (Brunet, 2020). For sparse canopies, L_w/h must depend on canopy density.

In the CSL (i.e., $z/h < 1$), L_{up} decreases with z (except that in near-neutral conditions it is roughly constant at $L_{\mathrm{up}} \approx h$), L_{do} increases with z and as a result L_{rms} is approximately constant with height (Figure 7a–c). The below-canopy behaviour of L_{up} and L_{do} can be explained with a near-neutral stratification in the below-canopy air space and a stable layer close to the canopy height that might result from strong radiative cooling of the canopy and possibly concurrent heat release from the soil at the forest floor (Jacobs *et al.,* 1994). Such temperature profiles were not uncommon during the two measurement campaigns, and are not uncommon in forests in general (Jacobs *et al.,* 1994; Dupont and Patton, 2012; Everard *et al.,* 2020; Schilperoort *et al.,* 2020). In such conditions, the θ isolines fluctuate vertically over the whole neutrally stratified air layer and hence $L_{\mathrm{do}} \approx z$ and $L_{\mathrm{up}} \approx z_{\mathrm{inv}} - z$ below the stably stratified inversion layer (residing at height z_{inv}) close to the canopy height. It remains an open question as to whether the observed below-canopy L_{rms} values indeed describe the effective vertical mixing length over which heat exchange takes place, or whether the below-canopy values obtained are merely artefacts of the measurement and length-scale estimation procedure. To be clear, an earlier study at the Hyytiälä site (Peltola *et al.,* 2021a) did find biases in the DTS-derived cross-canopy θ gradients, especially just after sunset, due to nonuniform longwave radiative cooling of the measurement cable at different heights, and these biases might disturb the length-scale estimation. Nevertheless, the below-canopy thermal plumes observed in stable conditions by Jacobs *et al.* (1994) and Dupont and Patton (2012) are in line with the below-canopy length-scale estimates here.

The isotropy ratio (i.e., the ratio between vertical and horizontal length scales, $L_{\mathrm{rms}}/L_{\mathrm{ho}}$) is below unity irrespective of height and stratification (Figure 8b), meaning that the eddies are flat and extend more horizontally than vertically. Above the canopy, L_{ho}/h varies between 0.7 and 1.5 slightly depending on stability and site, however it does not vary vertically (Figure 7d). With increasing stability,

L_{rms} decreases faster than L_{ho} (Figure 8b), since stratification primarily suppresses vertical motions and hence eddies flatten with increased stratification. There is a discrepancy between the two forests that might be due to a slightly incorrect value for eddy advection velocity U_{adv}. For example, Everard *et al.* (2021) showed that in canopy flows (in their study z/h varied between 0.2 and 2) U_{adv} was a constant fraction of local mean wind speed at all observation heights, indicative that U_{adv} increased with height (since wind speed increases with height). Their findings are in qualitative agreement with other U_{adv} profiles for sparse canopies (Huang *et al.*, 2009). Here, L_{ho} is estimated using wind data only at one height and hence the above-mentioned findings suggest that L_{ho} is underestimated (overestimated) above (below) that specific height. This could explain the discrepancy between sites as well.

5 | IMPLICATIONS FOR ABOVE- AND BELOW-CANOPY FLOWS

The findings on turbulence length scales presented above have implications for modelling and interpreting the turbulent canopy flows considered here. Specifically, these length scales are used to evaluate the RSL flow departure from M–O similarity and cross-canopy coupling using the Ω decoupling metric.

5.1 | RSL corrections for M–O similarity functions in above-canopy flows

The continuous profiles for L_{rms} and the theory presented in Section 2.2 (Equation 11) enable continuous profile estimates for the RSL modifications to M–O similarity functions (ϕ_h^*) from the data. We approximate the mixing length for heat (L_h) by L_{rms}. However, prior to utilizing Equation (11), the two unknowns (r_h and ϕ_h^{MO}) need to be estimated. In principle, they could be taken from the literature. However, we opt to estimate them from data measured above the RSL for self-consistency across the sites. This approach has an added advantage, because the uncertainty related to measurements and the findings in Equation (11) cancel out in the division (denominator and numerator are similarly biased). We assume that, at $z/h \approx 3.5$, the measurements are made above the RSL (hence $\phi_h^* \approx 1$ and $\phi_h \approx \phi_h^{MO}$, see Equation (10)) and estimate $r_h\phi_h^{MO}$ from Equation (9). Figure 9 shows $r_h\phi_h$ at two heights, along with an empirical fit to the values obtained above RSL. The fit asymptotes to $r_h\phi_h \approx 0.89$ as $\zeta \to 0$. This value is close to 0.77, which could be explained by $r_h = 1/\phi_w \approx 1/1.3 \approx 0.77$ and $\phi_h = 1$ and $Pr_t \approx 1$ (since $Pr_t = \phi_h/\phi_m$ and $\phi_m = 1$ when $\zeta \to 0$).

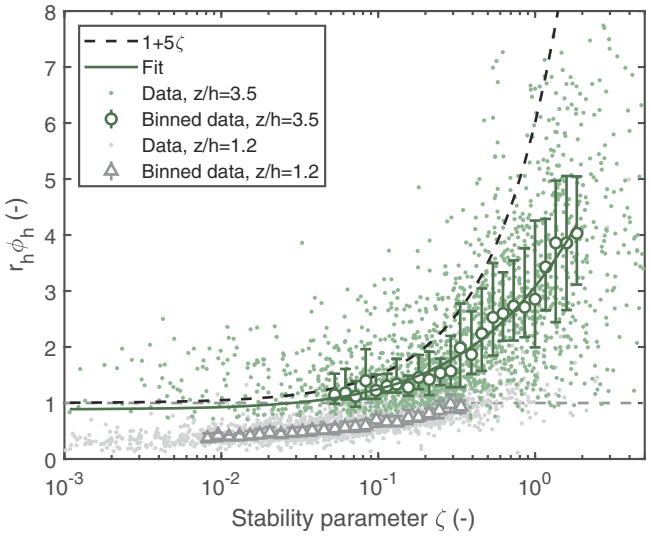

FIGURE 9 Dependence of $r_h\phi_h$ (estimated as $\kappa(z-d)/(\phi_w L_{rms})$, see Equation (9)) on the stability parameter ζ at two example heights in Hyytiälä. Filled markers show bin medians and error bars the interquartile range. A continuous line shows the nonlinear least-squares fit to bin medians above RSL ($r_h\phi_h = (0.80 + 6.98\zeta)^{0.55}$). The black dashed line shows the widely used estimate for the M–O similarity function ϕ_h (Kaimal and Finnigan, 1994). The data from $z/h = 1.2$ are below $z/h = 3.5$ and RSL effects on measured $r_h\phi_h$ are significant [Colour figure can be viewed at wileyonlinelibrary.com]

Based on Equation (7), this estimate renders $L_h = L_m = \kappa(z-d)$ if $r_m = 1/\phi_w$ is also assumed (see Appendix S1 and Basu and Holtslag (2021)). On the other hand, $r_h = 1$ and $\phi_h = 0.89$ (and hence $Pr_t = 0.89$) are also in line with the near-neutral value for $r_h\phi_h$. However, the literature values $r_h = 1/(\phi_w\phi_\theta) \approx 1/(1.3 \times 2) \approx 0.38$ and $\phi_h = 1$ (Kaimal and Finnigan, 1994) predict smaller value for $r_h\phi_h$ than were observed above the RSL (Figure 9). We hypothesise that this is due to ϕ_θ in the expression for r_h. The observed σ_θ upon which the literature ϕ_θ ($= \sigma_\theta/\theta_*$) values are based are increased by inactive turbulent motions, whereas these motions make a significantly smaller contribution to the heat transport (and θ_*). Hence, the literature values for ϕ_θ are likely inflated when compared with ϕ_θ calculated only from local (active) turbulence, in line with the theory in Section 2.2.

We estimate ϕ_h^* profiles based on Equation (11) using the empirical fit given above at all heights and at both sites when estimating L_h^{MO}. Near-neutral ϕ_h^* profiles are then estimated by fitting a curve similar to the one used for $r_h\phi_h$ and extrapolated to $\zeta \to 0$. Figure 10 shows the near-neutral ϕ_h^* profiles obtained. The profiles at the two sites are similar and show characteristics typical for CSL and RSL flows, that is, the values increase rapidly close to the canopy top and approach unity asymptotically near the RSL top. The observed ϕ_h^* at Hyytiälä reaches 0.95 at

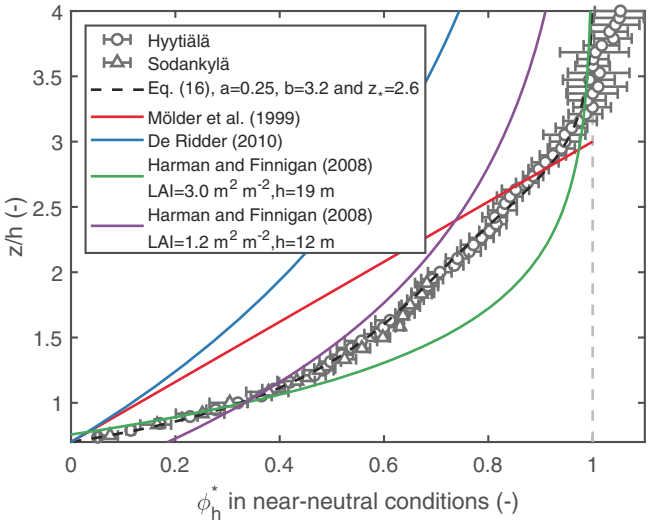

FIGURE 10 Dependence of roughness sublayer function φ_h^* on normalized height z/h. Markers show the values obtained based on observations (error bars relate to 95% confidence bounds), black dashed and dotted lines are empirical curves based on Equation (16), and the other lines show different estimates for ϕ^* in the literature. The Harman and Finnigan (2008) profiles are calculated using $c_{2c} = 0.5$, $\beta = 0.3$, $Sc = 0.5$, and $c_d = 0.2$. For Mölder *et al.* (1999) and De Ridder (2010) profiles, $3h$ was used as an estimate for RSL height. See more details in Section 5.1 [Colour figure can be viewed at wileyonlinelibrary.com]

$z/h \approx 3$, indicative of RSL height (note however that measurements at $z/h = 3.5$ were assumed to be above the RSL). The Harman and Finnigan (2008) model for ϕ_h^* agrees with the observed ϕ_h^* at the Hyytiälä site close to the canopy top and at the RSL top (Figure 10). This suggests that the model describes reasonably the departure of ϕ_h from M–O similarity theory in the RSL at this site. However, at the Sodankylä site the observed ϕ_h^* values are larger and approach unity faster as a function of z than was predicted by the Harman and Finnigan (2008) model. This could be due to the fact that the Sodankylä forest is hydrodynamically sparse and Hyytiälä dense (Brunet, 2020). That is, a dominance of mixing-layer type flow characteristics near the canopy top is expected only for dense canopies as assumed by Harman and Finnigan (2008), but not sparse canopies.

Reason for the similarity between the two observed ϕ_h^* profiles is unclear. Based on the Harman and Finnigan (2008) model, they should be different. Considering Equation (11), this finding suggests similar departure from the M–O predicted eddy sizes (i.e., $L_h \neq L_h^{MO}$) at the two sites. In Hyytiälä this departure could be attributed to mixing-layer eddies, whereas in Sodankylä it might be due to canopy disturbance of eddies attached to the forest floor and consequent creation of eddies that scale with h. Hence, the similar ϕ_h^* profiles would be a result of similar departure from M–O predicted eddy sizes at the two sites, despite different underlying physical mechanism (Hyytiälä: mixing-layer eddies, Sodankylä: breakage of attached eddies). However, more research is needed on sparse canopies before this hypothesis can be corroborated.

An empirical fit is made to the ϕ_h^* estimates using the formula

$$\phi_h^* = \frac{\kappa(z-d)}{\kappa(z-d) + \frac{ah}{1+e^{b(z/h-z_*)}}}, \tag{16}$$

where a , b , and z_* are fitting parameters (see Figure 10). This function is continuous and approaches unity at the RSL top and decays to zero at $z = d$. A *post hoc* interpretation of the fit can be made by recalling that $\phi_h^* = L_h^{MO}/L_h$ and hence $L_h^{MO} = \kappa(z-d)$ and $L_h = \kappa(z-d) + ah/(1+e^{b(z/h-z_*)})$. Similarly to Poggi *et al.* (2004), this formulation for L_h can be physically interpreted as a linear superposition of mixing lengths related to two independent processes, that is, boundary-layer and mixing-layer eddies, respectively. If $\kappa(z-d)$ is set to 0 when $z < d$, then this formulation gives $L_h \approx ah$ in the CSL, that is, below the canopy, since in such conditions $e^{b(z/h-z_*)} \approx 0$ with the estimated b and z_* values. This value for L_h can be related to the mixing-layer eddies residing at $z = h$ and could presumably be estimated independently utilizing canopy shear or the adjustment length scale Brunet (2020). The fit parameter z_* describes the height (in terms of z/h) at which the L_h departure from M–O similarity (i.e., $(ah)/(1+e^{b(z/h-z_*)})$) has decreased to half of its value found below the canopy (i.e., ah) and b describes how fast this departure decreases as z increases. The parameters b and z_* together dictate the depth of the air layer in which L_h departs from $\kappa(z-d)$ (i.e., RSL height).

5.2 | Coupling to the forest floor

A prior study (Peltola *et al.*, 2021b) conjectured that the flow is coupled to the surface when there are strong downdrafts able to reach the underlying surface despite forces hindering the vertical movement (buoyancy and drag force). The study also hypothesised that the proposed approach might provide a site-independent means to estimate flow decoupling when requiring a balance between background stratification, canopy drag, and vertical turbulent kinetic energy. The relative significance of these three terms is encoded in a decoupling metric Ω (Section 2.4). The length scales estimated here provide suitable means to test such a hypothesis as a function of Ω (Section 2.4).

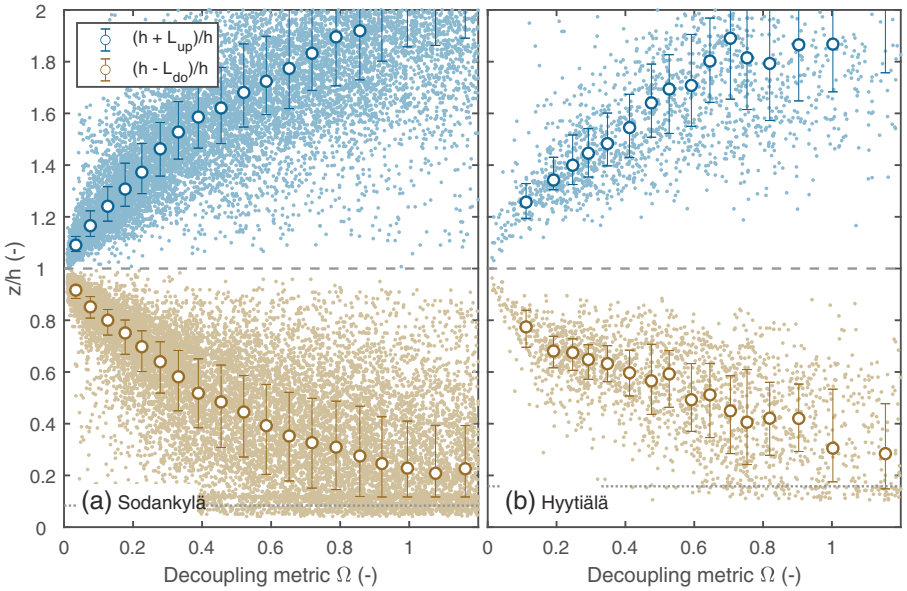

FIGURE 11 Dependence of L_{do} and L_{up} on the decoupling metric Ω at the two forest sites. Markers show bin medians and error bars the interquartile range. The horizontal dotted line denotes the lowest valid DTS measurement height [Colour figure can be viewed at wileyonlinelibrary.com]

Figure 11 shows the estimated L_{do} and L_{up} at $z = h$ as a function of Ω. The markers depict the bottom and top of the eddy (see Figure 1) relative to $z = h$ and these can be considered as the vertical limits of the domain over which the eddy residing at $z = h$ is in interaction with other eddies within the canopy volume. When the markers reach $z = 0$, the eddy is in direct interaction with (and is coupled to) the forest floor. At Sodankylä, the eddy size (difference between markers in Figure 11) increases approximately linearly with increasing Ω and the eddy couples with the ground surface when $\Omega \approx 0.6$–0.8. This agrees with a prior study that heuristically defined flow coupling to take place when $\Omega \approx 0.61$ (Peltola *et al.,* 2021b).

At the denser Hyytiälä site, the length-scale dependence on Ω is less clear and the scatter is more pronounced. Nevertheless, the eddy size also increases with increasing Ω at this site. Hyytiälä has a pronounced canopy layer where branches and needles block the air flow and below it a relatively open trunk space exists where the air flow is not similarly hindered by drag. Hence, hindrance of vertical movement is mostly confined to the crown layer. When deriving Ω, Peltola *et al.* (2021b) assumed constant canopy density with height. This discrepancy between the site characteristics and assumptions made in the derivation might explain why $h - L_{do}$ remains approximately constant around $0.6z/h$ when Ω is between 0.2 and 0.6 (Figure 11b). At this particular height, the eddy penetration downwards might be hindered by the canopy drag, since most of the canopy elements are confined to the topmost part of the forest, whereas Ω assumes that canopy density is constant with height. Nevertheless, at Hyytiälä $h - L_{do}$ reaches the lowest DTS measurement height when $\Omega \approx 0.6$–1, albeit the scatter is evident.

These results strengthen the theoretical basis of Ω and its usability as a decoupling metric at forested measurement sites but do not corroborate fully the site-independent Ω threshold value for coupling as conjectured earlier (Peltola *et al.,* 2021b). These results have practical implications for eddy covariance (EC) flux data filtering during stably stratified nocturnal conditions. Currently, decoupled periods are identified in the EC data processing routines with a threshold value for u_* (Goulden *et al.,* 1996; Pastorello *et al.,* 2020) and filtered from EC flux time series. However, the heuristic u_* approach lacks any connection to the forces hindering the vertical coupling. Here, filtering based on Ω might offer a theoretical basis and an improvement.

6 | CONCLUSIONS

Spatially continuous high-frequency potential temperature profiles were utilized at two Scots pine forest sites to derive and explore turbulence (thermal) length-scale profiles in stably stratified situations. The length scales were derived from the θ profiles by assuming that the θ isoline fluctuations in the profiles were related to adiabatic vertically displaced air parcels akin to the Prandtl mixing-length hypothesis. The proposed framework to derive the length scales is, in theory, also applicable to daytime unstably stratified conditions, however in practice it is difficult to apply, since elevated profiles are needed in such conditions (daytime eddies can reach the ABL height). The whole eddy needs to be captured by the profile to derive meaningful estimates of the length scales with the method. For example, DTS cables affixed to a

tethered balloon (Lapo *et al.,* 2022) might provide extensive enough elevation for resolving daytime eddies with the method and/or capturing the whole surface layer in near-neutral conditions.

The results here have implications for practical evaluation of the coupling between the forest-floor and above-canopy air layers. This is becoming essential for reliable eddy covariance measurements, as forest-floor fluxes are a major contributor to biosphere–atmosphere exchange. A necessary requirement for the coupling appears to be the existence of strong downdrafts that are able to penetrate through the canopy and stably stratified air layers and hence interact with the ground. This is in line with the derivation of the decoupling metric Ω in a prior study (Peltola *et al.,* 2021b). The findings here on DTS derived eddy length scales consolidate the departure of RSL flows from M–O similarity as related to large coherent eddies that do not scale with height in the manner described by M–O theory. Based on this, we were able to derive a detailed profile of the RSL corrections for M–O similarity and show that the Harman and Finnigan (2008) model described this departure adequately above a dense canopy, but was inaccurate above a sparse canopy. These results have implications for the inclusion of RSL processes in numerical weather prediction and Earth system models. Finally, data collected and analysed here are made openly available and they should prove useful, for example, in the development of canopy flow processes for large-eddy simulations (Peltola, 2022a, 2022b).

AUTHOR CONTRIBUTIONS

Olli Peltola: conceptualization; data curation; formal analysis; funding acquisition; investigation; methodology; project administration; software; visualization; writing – original draft; writing – review and editing. **Mika Aurela:** investigation; methodology; resources; writing – review and editing. **Samuli Launiainen:** conceptualization; writing – review and editing. **Gabriel Katul:** conceptualization; writing – review and editing.

ACKNOWLEDGEMENTS

O.P. has been supported by a postdoctoral researcher project (Grant no. 315424) funded by the Academy of Finland. G.K. acknowledges support from the US National Science Foundation (NSF-AGS-2028633 and NSF-IOS-1754893) and the US Department of Energy (DE-SC0022072). S.L. acknowledges support from the Academy of Finland (296116). The technicians at the Hyytiälä research station, Tuukka Keränen, and Pasi Kolari are thanked for their help during the Hyytiälä campaign and Timo Mäkelä, Juuso Rainne, Juha Hatakka, Tuukka Keränen, and Irene Suomi for their assistance during the Sodankylä campaign. Tuomas Laurila and Timo Vesala are thanked for enabling these two measurement campaigns.

ORCID

Olli Peltola https://orcid.org/0000-0002-1744-6290

REFERENCES

Abolafia-Rosenzweig, R., He, C., Burns, S.P. and Chen, F. (2021) Implementation and evaluation of a unified turbulence parameterization throughout the canopy and roughness sublayer in Noah-MP snow simulations. *Journal of Advances in Modeling Earth Systems*, 13, e2021MS002665. https://doi.org/10.1029/2021MS002665.

Arnqvist, J. and Bergström, H. (2015) Flux-profile relation with roughness sublayer correction. *Quarterly Journal of the Royal Meteorological Society*, 141, 1191–1197. https://doi.org/10.1002/qj.2426.

Aubinet, M. (2008) Eddy covariance CO_2 flux measurements in nocturnal conditions: an analysis of the problem. *Ecological Applications*, 18, 1368–1378. https://doi.org/10.1890/06-1336.1.

Baas, P., de Roode, S.R. and Lenderink, G. (2008) The scaling behaviour of a turbulent kinetic energy closure model for stably stratified conditions. *Boundary-Layer Meteorology*, 127, 17–36. https://doi.org/10.1007/s10546-007-9253-y.

Basu, S. and Holtslag, A.A.M. (2021) Turbulent Prandtl number and characteristic length scales in stably stratified flows: steady-state analytical solutions. *Environmental Fluid Mechanics*, 21, 1273–1302. https://doi.org/10.1007/s10652-021-09820-7.

Blackadar, A.K. (1962) The vertical distribution of wind and turbulent exchange in a neutral atmosphere. *Journal of Geophysical Research*, 67, 3095–3102. https://doi.org/10.1029/JZ067i008p03095.

Bonan, G.B., Patton, E.G., Harman, I.N., Oleson, K.W., Finnigan, J.J., Lu, Y. and Burakowski, E.A. (2018) Modeling canopy-induced turbulence in the earth system: a unified parameterization of turbulent exchange within plant canopies and the roughness sublayer (CLM-ml v0). *Geoscientific Model Development*, 11, 1467–1496.

Brock, F.V. (1986) A nonlinear filter to remove impulse noise from meteorological data. *Journal of Atmospheric and Oceanic Technology*, 3, 51–58. https://doi.org/10.1175/1520-0426(1986)003<0051:ANFTRI>2.0.CO;2.

Brost, R.A. and Wyngaard, J.C. (1978) A model study of the stably stratified planetary boundary layer. *Journal of the Atmospheric Sciences*, 35, 1427–1440. https://doi.org/10.1175/1520-0469(1978)035<1427:AMSOTS>2.0.CO;2.

Brunet, Y. (2020) Turbulent flow in plant canopies: historical perspective and overview. *Boundary-Layer Meteorology*, 177, 315–364. https://doi.org/10.1007/s10546-020-00560-7.

Cava, D., Giostra, U., Siqueira, M. and Katul, G. (2004) Organised motion and radiative perturbations in the nocturnal canopy sublayer above an even-aged pine forest. *Boundary-Layer*

Meteorology, 112, 129–157. https://doi.org/10.1023/B:BOUN.0000020160.28184.a0.

Cava, D., Katul, G.G., Scrimieri, A., Poggi, D., Cescatti, A. and Giostra, U. (2006) Buoyancy and the sensible heat flux budget within dense canopies. *Boundary-Layer Meteorology*, 118, 217–240. https://doi.org/10.1007/s10546-005-4736-1.

De Ridder, K. (2010) Bulk transfer relations for the roughness sublayer. *Boundary-Layer Meteorology*, 134, 257–267. https://doi.org/10.1007/s10546-009-9450-y.

Deardorff, J.W. (1980) Stratocumulus-capped mixed layers derived from a three-dimensional model. *Boundary-Layer Meteorology*, 18, 495–527. https://doi.org/10.1007/BF00119502.

Des Tombe, B., Schilperoort, B. and Bakker, M. (2020) Estimation of temperature and associated uncertainty from fiber-optic Raman-Spectrum distributed temperature sensing. *Sensors*, 20, 2235.

Dupont, S. and Patton, E.G. (2012) Momentum and scalar transport within a vegetation canopy following atmospheric stability and seasonal canopy changes: the CHATS experiment. *Atmospheric Chemistry and Physics*, 12, 5913–5935.

Edwards, J.M., Beljaars, A.C.M., Holtslag, A.A.M. and Lock, A.P. (2020) Representation of boundary-layer processes in numerical weather prediction and climate models. *Boundary-Layer Meteorology*, 177, 511–539. https://doi.org/10.1007/s10546-020-00530-z.

Epps, B.P. and Krivitzky, E.M. (2019) Singular value decomposition of noisy data: noise filtering. *Experiments in Fluids*, 60, 126. https://doi.org/10.1007/s00348-019-2768-4.

Everard, K.A., Katul, G.G., Lawrence, G.A., Christen, A. and Parlange, M.B. (2021) Sweeping effects modify Taylor's frozen turbulence hypothesis for scalars in the roughness sublayer. *Geophysical Research Letters*, 48, e2021GL093746. https://doi.org/10.1029/2021GL093746.

Everard, K.A., Oldroyd, H.J. and Christen, A. (2020) Turbulent heat and momentum exchange in Nocturnal drainage flow through a sloped vineyard. *Boundary-Layer Meteorology*, 175, 1–23. https://doi.org/10.1007/s10546-019-00491-y.

Finnigan, J. (2000) Turbulence in plant canopies. *Annual Review of Fluid Mechanics*, 32, 519–571. https://doi.org/10.1146/annurev.fluid.32.1.519.

Finnigan, J., Shaw, R.H. and Patton, E.G. (2009) Turbulence structure above a vegetation canopy. *Journal of Fluid Mechanics*, 637, 387–424.

Gao, W., Shaw, R.H. and Paw U, K.T. (1989) Observation of organized structure in turbulent flow within and above a forest canopy. *Boundary-Layer Meteorology*, 47, 349–377. https://doi.org/10.1007/BF00122339.

Garratt, J.R. (1980) Surface influence upon vertical profiles in the atmospheric near-surface layer. *Quarterly Journal of the Royal Meteorological Society*, 106, 803–819. https://doi.org/10.1002/qj.49710645011.

Goulden, M.L., Munger, J.W., Fan, S.M., Daube, B.C. and Wofsy, S.C. (1996) Measurements of carbon sequestration by long-term eddy covariance: methods and a critical evaluation of accuracy. *Global Change Biology*, 2, 169–182.

Harman, I.N. and Finnigan, J.J. (2007) A simple unified theory for flow in the canopy and roughness sublayer. *Boundary-Layer Meteorology*, 123, 339–363. https://doi.org/10.1007/s10546-006-9145-6.

Harman, I.N. and Finnigan, J.J. (2008) Scalar concentration profiles in the canopy and roughness sublayer. *Boundary-Layer Meteorology*, 129, 323–351. https://doi.org/10.1007/s10546-008-9328-4.

Huang, J. and Bou-Zeid, E. (2013) Turbulence and vertical fluxes in the stable atmospheric boundary layer. Part I: a large-eddy simulation study. *Journal of the Atmospheric Sciences*, 70, 1513–1527.

Huang, J., Cassiani, M. and Albertson, J.D. (2009) The effects of vegetation density on coherent turbulent structures within the canopy sublayer: a large-eddy simulation study. *Boundary-Layer Meteorology*, 133, 253–275. https://doi.org/10.1007/s10546-009-9423-1.

Ivey, G.N., Winters, K.B. and De Silva, I.P.D. (2000) Turbulent mixing in a sloping benthic boundary layer energized by internal waves. *Journal of Fluid Mechanics*, 418, 59–76.

Jacobs, A.F.G., Van Boxel, J.H. and El-Kilani, R.M.M. (1994) Nighttime free convection characteristics within a plant canopy. *Boundary-Layer Meteorology*, 71, 375–391. https://doi.org/10.1007/BF00712176.

Kaimal, J.C. and Finnigan, J.J. (1994) *Atmospheric Boundary Layer Flows: Their Structure and Measurement*. New York: Oxford University Press. http://helka.linneanet.fi/cgi-bin/Pwebrecon.cgi?BBID=636956.

Karttunen, S., O'Connor, E., Peltola, O. and Järvi, L. (2022) Quantifying the coastal urban surface layer structure using distributed temperature sensing in Helsinki, Finland. *Atmos. Meas. Tech.*, 15, 2417–2432. https://doi.org/10.5194/amt-15-2417-2022

Katul, G.G., Geron, C.D., Hsieh, C.-I., Vidakovic, B. and Guenther, A.B. (1998) Active turbulence and scalar transport near the forest-atmosphere interface. *Journal of Applied Meteorology*, 37, 1533–1546. https://doi.org/10.1175/1520-0450(1998)037<1533:ATASTN>2.0.CO.

Katul, G.G., Porporato, A., Shah, S. and Bou-Zeid, E. (2014) Two phenomenological constants explain similarity laws in stably stratified turbulence. *Physical Review E*, 89, 23007. https://doi.org/10.1103/PhysRevE.89.023007.

Kolari, P., Aalto, J., Levula, J., Kulmala, L., Ilvesniemi, H. and Pumpanen, J. (2022) *Hyytiälä SMEAR II site characteristics*. https://doi.org/10.5281/zenodo.5909681.

Lapo, K., Freundorfer, A., Fritz, A., Schneider, J., Olesch, J., Babel, W. and Thomas, C.K. (2022) The large eddy observatory, Voitsumra experiment 2019 (LOVE19) with high-resolution, spatially distributed observations of air temperature, wind speed, and wind direction from fiber-optic distributed sensing, towers, and ground-based remote sensing. *Earth System Science Data*, 14, 885–906.

Lee, J., Hong, J., Noh, Y. and Jiménez, P.A. (2020) Implementation of a roughness sublayer parameterization in the weather research and forecasting model (WRF version 3.7.1) and its evaluation for regional climate simulations. *Geoscientific Model Development*, 13, 521–536.

Li, D. (2021) The O'KEYPS equation and 60 years beyond. *Boundary-Layer Meteorology*, 179, 19–42. https://doi.org/10.1007/s10546-020-00585-y.

Lorke, A. and Wüest, A. (2002) Probability density of displacement and overturning length scales under diverse stratification. *Journal of Geophysical Research: Oceans*, 107, 7-1–7-11. https://doi.org/10.1029/2001JC001154.

MacDonald, M. and Teixeira, J. (2020) Scaling behavior of a turbulent kinetic energy closure scheme for the stably stratified atmosphere: a steady-state Analysis. *Journal of the Atmospheric Sciences*, 77, 3161–3170. https://journals.ametsoc.org/view/journals/atsc/77/9/jasD1903%32.xml.

Maroneze, R., Acevedo, O.C., Costa, F.D., Puhales, F.S., Anabor, V., Lemes, D.N. and Mortarini, L. (2020) How is the two-regime stable boundary layer reproduced by the different turbulence parametrizations in the weather research and forecasting model? *Boundary-Layer Meteorology.*, 178, 383–413. https://doi.org/10.1007/s10546-020-00581-2.

Marusic, I. and Monty, J.P. (2019) Attached Eddy model of wall turbulence. *Annual Review of Fluid Mechanics*, 51, 49–74. https://doi.org/10.1146/annurev-fluid-010518-040427.

Mölder, M., Grelle, A., Lindroth, A. and Halldin, S. (1999) Flux-profile relationships over a boreal forest—roughness sublayer corrections. *Agricultural and Forest Meteorology*, 98-99, 645–658. http://www.sciencedirect.com/science/article/pii/S01681923990%01318.

Monin, A. and Obukhov, A. (1954) Basic laws of turbulent mixing in the atmosphere near the ground. *Trudy Geofiz Inst AN SSSR*, 24, 163–187.

Moum, J.N. (1996) Energy-containing scales of turbulence in the ocean thermocline. *Journal of Geophysical Research: Oceans*, 101, 14095–14109. https://doi.org/10.1029/96JC00507.

Pastorello, G., Trotta, C., Canfora, E., Chu, H., Christianson, D., Cheah, Y.-W., Poindexter, C., Chen, J., Elbashandy, A., Humphrey, M., Isaac, P., Polidori, D., Reichstein, M., Ribeca, A., van Ingen, C., Vuichard, N., Zhang, L., Amiro, B., Ammann, C., Arain, M.A., Ardö, J., Arkebauer, T., Arndt, S.K., Arriga, N., Aubinet, M., Aurela, M., Baldocchi, D., Barr, A., Beamesderfer, E., Marchesini, L.B., Bergeron, O., Beringer, J., Bernhofer, C., Berveiller, D., Billesbach, D., Black, T.A., Blanken, P.D., Bohrer, G., Boike, J., Bolstad, P.V., Bonal, D., Bonnefond, J.-M., Bowling, D.R., Bracho, R., Brodeur, J., Brümmer, C., Buchmann, N., Burban, B., Burns, S.P., Buysse, P., Cale, P., Cavagna, M., Cellier, P., Chen, S., Chini, I., Christensen, T.R., Cleverly, J., Collalti, A., Consalvo, C., Cook, B.D., Cook, D., Coursolle, C., Cremonese, E., Curtis, P.S., D'Andrea, E., da Rocha, H., Dai, X., Davis, K.J., Cinti, B.D., de Grandcourt, A., Ligne, A.D., De Oliveira, R.C. and Delpierre, N. (2020) The FLUXNET2015 dataset and the ONEFlux processing pipeline for eddy covariance data. *Scientific Data*, 7, 225. https://doi.org/10.1038/s41597-020-0534-3.

Peltola, O., Lapo, K., Martinkauppi, I., O'Connor, E., Thomas, C.K. and Vesala, T. (2021a) Suitability of fibre-optic distributed temperature sensing for revealing mixing processes and higher-order moments at the forest-air interface. *Atmospheric Measurement Techniques*, 14, 2409–2427.

Peltola, O., Lapo, K. and Thomas, C.K. (2021b) A physics-based universal indicator for vertical decoupling and mixing across canopies architectures and dynamic stabilities. *Geophysical Research Letters*, 48, e2020GL091615.

Peltola, O. (2022a). High frequency distributed temperature sensing and eddy covariance data observed at Sodankylä measurement station during summer/winter 2020 [Data set]. Zenodo. https://doi.org/10.5281/zenodo.6591446

Peltola, O. (2022b). High frequency distributed temperature sensing and eddy covariance data observed at Hyytiälä measurement station during summer 2019 [Data set]. Zenodo. https://doi.org/10.5281/zenodo.6591453

Physick, W.L. and Garratt, J.R. (1995) Incorporation of a high-roughness lower boundary into a mesoscale model for studies of dry deposition over complex terrain. *Boundary-Layer Meteorology*, 74, 55–71. https://doi.org/10.1007/BF00715710.

Poggi, D., Porporato, A., Ridolfi, L., Albertson, J.D. and Katul, G.G. (2004) The effect of vegetation density on canopy sub-layer turbulence. *Boundary-Layer Meteorology*, 111, 565–587. https://doi.org/10.1023/B:BOUN.0000016576.05621.73.

Prandtl, L. (1925) 7. Bericht über Untersuchungen zur ausgebildeten Turbulenz. *ZAMM - Journal of Applied Mathematics and Mechanics/Zeitschrift für Angewandte Mathematik und Mechanik*, 5, 136–139. https://doi.org/10.1002/zamm.19250050212.

Raupach, M.R., Finnigan, J.J. and Brunei, Y. (1996) Coherent eddies and turbulence in vegetation canopies: the mixing-layer analogy. *Boundary-Layer Meteorology*, 78, 351–382. https://doi.org/10.1007/BF00120941.

Raupach, M.R. and Thom, A.S. (1981) Turbulence in and above plant canopies. *Annual Review of Fluid Mechanics*, 13, 97–129. https://doi.org/10.1146/annurev.fl.13.010181.000525.

Salesky, S.T., Katul, G.G. and Chamecki, M. (2013) Buoyancy effects on the integral lengthscales and mean velocity profile in atmospheric surface layer flows. *Physics of Fluids*, 25, 105101. https://doi.org/10.1063/1.4823747.

Sandu, I., Beljaars, A., Bechtold, P., Mauritsen, T. and Balsamo, G. (2013) Why is it so difficult to represent stably stratified conditions in numerical weather prediction (NWP) models? *Journal of Advances in Modeling Earth Systems*, 5, 117–133. https://doi.org/10.1002/jame.20013.

Schilperoort, B., Coenders-Gerrits, M., Rodríguez, C.J., van der Tol, C., van de Wiel, B. and Savenije, H. (2020) Decoupling of a Douglas fir canopy: a look into the subcanopy with continuous vertical temperature profiles. *Biogeosciences Discussions*, 17, 6423–6439.

Smyth, W.D. and Moum, J.N. (2000) Length scales of turbulence in stably stratified mixing layers. *Physics of Fluids*, 12, 1327–1342. https://doi.org/10.1063/1.870385.

Sorbjan, Z. (2006) Local structure of turbulence in stably stratified boundary layers. *Journal of the Atmospheric Sciences*, 63, 1526–1537. https://doi.org/10.1175/JAS3704.1.

Sorbjan, Z. and Balsley, B.B. (2008) Microstructure of turbulence in the stably stratified boundary layer. *Boundary-Layer Meteorology*, 129, 191–210. https://doi.org/10.1007/s10546-008-9310-1.

Thomas, C. and Foken, T. (2007) Organised motion in a tall spruce canopy: temporal scales, structure spacing and terrain effects. *Boundary-Layer Meteorology*, 122, 123–147. https://doi.org/10.1007/s10546-006-9087-z.

Thomas, C.K. and Selker, J. (2021) Optical fiber-based distributed sensing methods. In: Foken, T. (Ed.) *Springer Handbook of Atmospheric Measurements*. Cham: Springer International Publishing., pp. 609–631. https://doi.org/10.1007/978-3-030-52171-4_20.

Thorpe, S.A. (1977) Turbulence and mixing in a Scottish loch. *Philosophical Transactions of the Royal Society of London. Series A, Mathematical and Physical Sciences*, 286, 125–181. https://doi.org/10.1098/rsta.1977.0112.

van de Giesen, N., Steele-Dunne, S.C., Jansen, J., Hoes, O., Hausner, M.B., Tyler, S. and Selker, J. (2012) Double-ended calibration of fiber-optic Raman spectra distributed temperature sensing data. *Sensors*, 12, 5471–5485.

Wilczak, J.M., Oncley, S.P. and Stage, S.A. (2001) Sonic anemometer tilt correction algorithms. *Boundary-Layer Meteorology*, 99, 127–150. https://doi.org/10.1023/A:1018966204465.

SUPPORTING INFORMATION

Additional supporting information can be found online in the Supporting Information section at the end of this article.

How to cite this article: Peltola, O., Aurela, M., Launiainen, S. & Katul, G. (2022) Probing eddy size and its effective mixing length in stably stratified roughness sublayer flows. *Quarterly Journal of the Royal Meteorological Society*, 148(749), 3756–3773. Available from: https://doi.org/10.1002/qj.4386